

The effect of horizontal plasma inhomogeneities in 3D NLTE radiation transfer in stellar atmospheres

A. Tichý^{a,b}, J. Kubát^{b,*}

^a*Ústav teoretické fyziky a astrofyziky, Masarykova univerzita, Kotlářská 2, CZ-611 37 Brno, Czech Republic*

^b*Astronomický ústav, Akademie věd České republiky, Fričova 298, CZ-251 65 Ondřejov, Czech Republic*

Abstract

We aim to demonstrate the effect of atmospheric inhomogeneities on the emergent specific intensity and radiation flux of a spectral line radiation. We self-consistently solve the NLTE problem for a two-level atom in a 3D atmosphere using the Cartesian grid. For that purpose, we use the 3D radiative transfer code PORTA. By examining simple examples, we study cases where the temperature inhomogeneities in the atmosphere models lead to the modification of the emergent radiation. We show that specific temperature inhomogeneities in the model atmospheres influence the emerging radiation, and that interpretation of the stellar spectra based on a plane-parallel atmosphere models can lead to erroneous conclusions about the atmospheric structure.

Keywords: radiative transfer, line: formation, stars: atmospheres

1. Introduction

It has been known from the onset of the modern radiative transfer theory that geometry of the medium plays a significant role in radiative transfer problems (e.g. Cram, 1977; Auer, 2003). However, in most common cases of models of stellar atmospheres, the assumption of one-dimensionality, either in the case of plane parallel or spherically symmetric medium, is the most natural one given the lack of spatial resolution of the observations and the numerical complexity of the multi-dimensional models (see, e.g., Hubeny & Mihalas, 2015, Chapter 16). Real stellar atmospheres are not so geometrically simple, they can be quite inhomogeneous in all spatial directions, which can lead to significant failure of the diagnostics based upon the 1D models.

Although there is a growing number of 3D radiative transfer calculations (e.g. Ibgui et al. 2013

and references therein, Leenaarts et al. 2013a,b), at the same time the much simpler 1D approximation is being widely used. Uitenbroek & Criscuoli (2011) have pointed out three main reasons for which the 1D models can fail explaining the emergent spectra: (i) nonlinearity in the Planck function with temperature, affecting the average intensity of the emergent radiation through thermal contributions to local source functions in the area of formation; (ii) nonlinearities in molecular formation with inhomogeneities in temperature and density, which enhance abundances in inhomogeneous atmosphere with respect to a homogeneous 1D atmosphere with the same average properties; and (iii) anisotropies caused by convective motions, which have a strong impact on the resulting center-to-limb variation of line-center intensities.

Although inhomogeneities require a 3D treatment to correctly describe the transfer of radiation, they are very often treated in 1D approximation basically to make the problem tractable. Typical examples are studies of clumping in stellar atmospheres and winds, where the inhomogeneous

*Corresponding author

Email address: kubat@sunstel.asu.cas.cz
(J. Kubát)

geneities are believed to be a consequence of radiative-acoustic instability (Owocki et al. 1988, see also the review Sundqvist et al. 2012), adiabatic fluctuations (Chiueh, 1997) or subphotospheric convection (Cantiello et al., 2009). As it was shown by Šurlan et al. (2012, 2013) (see also Oskinova et al., 2016), proper 3D treatment of inhomogeneities is necessary to take into account both optically thin and optically thick clumps.

In this paper, we describe a phenomenon related to the NLTE effects in the spectral line formation due to small-scale inhomogeneities in the thermal structure of a stellar atmosphere that can significantly modify the shape of spectral lines. We show that interpreting a spectrum in terms of one-dimensional model atmospheres can lead to erroneous conclusions about the atmospheric structure.

In Section 2, we formulate the problem and describe in detail physical properties of employed model atmospheres, and summarize used numerical methods. Selected results of our calculations are shown and explained in Section 3, followed by a direct application on a simplified model of a spherical star in Section 4. Conclusions are presented in Section 5.

2. Model atmosphere and setting the line-formation problem

We study the radiation transfer in an academic spectral line at wavelength $\lambda_0 = 5000 \text{ \AA}$, forming between the lower level ℓ and the upper level u of a two-level atom. The atomic angular momenta are $J_\ell = 0$ and $J_u = 1$, the Einstein coefficient of a spontaneous emission is taken as $A_{u\ell} = 10^8 \text{ s}^{-1}$. For the sake of simplicity, we fix the collisional destruction probability $\epsilon = C_{u\ell}/(A_{u\ell} + C_{u\ell}) = 10^{-4}$, where $C_{u\ell}$ is the collisional deexcitation rate.

We do not consider background continuum opacity and emissivity in our model. The line source function, which directly enters the radiative transfer equation, is at each point of the medium given by contribution of thermal emission and locally scattered radiation. In the case of a plasma composed of two-level atoms it reads (Hubeny & Mihalas,

2015, Eq. 14.34)

$$S = (1 - \epsilon)J + \epsilon B(T), \quad (1)$$

where $B(T)$ is the Planck function and J is the line-profile integrated (mean) intensity of the locally scattered radiation.

We solve the radiative transfer using cartesian coordinates x , y , and z in a box with dimensions D_x , D_y , and D_z . The coordinate z describes the vertical direction in the atmosphere. We use the complex Voigt function as the absorption profile and calculate radiation for 101 discrete frequency points. The spectral line is thermalized at the bottom of the model atmosphere ($z = z_0$) and the line source function is therefore equal to the Planck function there, i.e., $S(x, y, z_0) = B(T(x, y, z_0))$ for all x and y .

We construct a grid of 3D model atmospheres with different horizontal variations of temperature. The atomic volume density in all the models is exponentially stratified following the expression

$$\overline{N(z)} = N_0 \exp\left(-\frac{z - z_0}{\beta}\right). \quad (2)$$

In all our calculations we set the density scale height $\beta = 75 \text{ km}$ and $N_0 = 10^{12} \text{ cm}^{-3}$. The vertical extension of the atmosphere $D_z = 2000 \text{ km}$ and we set $z_0 = 0 \text{ km}$. The structure and adopted values are chosen to represent a Sun-like stationary atmosphere, while the distribution (2) corresponds to stratification established by gravitational and buoyancy forces.

In order to mimic the temperature variation of the inhomogeneous stellar atmosphere we impose sinusoidal variation of kinetic temperature in the horizontal directions,

$$T(x, y) = T_0 \left[1 + \alpha_T \sin\left(2\pi \frac{kx}{D_x}\right) \sin\left(2\pi \frac{ky}{D_y}\right) \right]. \quad (3)$$

This means that the mean temperature at any height z (including the very bottom layer at z_0 , where the perturbation in temperature is also assumed) in a model atmosphere is equal to T_0 . We assume periodic boundary conditions in the horizontal directions of the model. The dimensionless parameter $\alpha_T \in \langle 0, 1 \rangle$ quantifies the amplitude of the temperature perturbation: The case

of $\alpha_T = 0$ corresponds to the 1D isothermal atmosphere while in the case $\alpha_T = 1$ the perturbation is maximum. The dimensionless parameter k determines the spatial period of the perturbation. For the sake of simplicity, we assume the same periods along the x and y axes. For numerical convenience, the horizontal dimensions of the model mesh is always set so that it is equal to one period of the fluctuation. The actual domain size in km therefore depends on k . In the $k = 1$ case, the horizontal domain size is $D_x \times D_y = 1000 \text{ km} \times 1000 \text{ km}$. For convenience, the spatial dimensions are hereafter expressed in $\text{Mm} = 10^6 \text{ m}$. In all our calculations, we use $T_0 = 6000 \text{ K}$.

Similarly to Eq. (3), one could also introduce horizontal inhomogeneities in density into the models (considering them separately, or simultaneously in phase or anti-phase), and study their impact on the emergent radiation. We did so for the purpose of a wider parametric study of the problem of inhomogeneous 3D atmospheres. However, we found that the effect of horizontal density distribution on line opacity (and thus the height of formation) imposes negligible changes in the resulting intensity spectrum, compared to the effect of temperature inhomogeneities on source function. Therefore we decided to concentrate on the effect of temperature perturbations.

Numerically, the mesh of the model is a cartesian grid with $100 \times 100 \times 120$ points along the x , y , and z axes, respectively. The numerical solution of the NLTE problem is found using the code PORTA (Štěpán & Trujillo Bueno, 2013).

PORTA is a computer program designed for solving the problem of generation and transfer of spectral line intensity and polarization in three-dimensional models of stellar atmospheres. The numerical methods of the solution implemented in PORTA are highly convergent even in complex physical environments with steep gradients of physical variables and anisotropic radiation. The implemented 3D formal solver of radiative transfer equation uses monotonic Bézier interpolation of source function along radiation beams within the short-characteristic scheme. Among the best advantages is its efficient parallelization strategy, allowing simulation of radiation transfer

using reasonably realistic 3D models. The time needed to calculate one of our NLTE models (i.e. a model atmosphere with a fixed thermodynamic structure, for which we solve the NLTE problem) was variable depending on specific properties of the model, typical calculation time was 3 – 5 days using 61 cores. We have calculated several tens of models with various inhomogeneity amplitudes and periods, while searching for the conditions under which the emergent radiation is affected.

After the self-consistent solution of the NLTE problem is found, we calculate the formal solution of the radiative transfer equation at each surface point of the model atmosphere. We thus obtain the resulting intensity at all wavelengths at each surface point (x_i, y_j) , $i, j = 1, 2, \dots, N$, where N is the number of grid nodes per x - and y - axes. From that information, we can construct synthetic spectrum of the considered line.

The impact of horizontal inhomogeneities on the spectral line profile diminishes in the limiting cases of $k \rightarrow 0$ and $k \rightarrow \infty$. On the other hand, the most significant impact of the horizontal radiation transfer can be expected if the spatial period of the perturbation is comparable to the mean photon destruction path ℓ^* , which a photon can travel (while being absorbed and re-emitted) before it becomes effectively destroyed (see, e.g. Hubeny & Mihalas, 2015, Chapter 14.2). In such case, regions of the atmosphere with different thermal properties can interact radiatively. As we show below, the line-of-sight (LOS) effects can also play important role in depth of formation of the near wings of the line if $k \approx 1$ (discussed in Section 4.2). In our models, we study the sensitivity of the line profile for $k \in [0.1, 10]$.

We intentionally try to keep the models as simple as possible, in order to study solely the impact of inhomogeneous thermal structure of an atmosphere on the emergent radiation. Horizontal temperature inhomogeneities introduced by Eq. (3) are supposed to represent a physical asymmetry in thermodynamic structure of an atmosphere, which can be caused by, e.g., convective motions, stellar oscillation modes or MHD driven phenomena, as long as the necessary conditions are met (for instance the presence of surface mag-

netic field, macroscopic motions and/or any geometrical asymmetry might have to be taken into account). However, our models are purely academic, and are aimed to demonstrate the diagnostic power of 3D radiation transfer when studying such effects. More realistic models should be implemented for a direct application in stellar astrophysics.¹

3. Intensity of the emergent radiation

In the following sections, we study the impact of temperature inhomogeneities on the emergent radiation intensity spectrum. We intend to (a) find differences with respect to the unperturbed model; (b) investigate the impact of 1D approximation on determination of the thermal stratification of the atmosphere. Since the 1D stellar atmosphere usually serves as an approximate representation instead of a generally more realistic 3D case (where the solution of the NLTE problem is significantly more time-costly and technically difficult), we want to stress possible limitations of such simplification.

3.1. Spatially resolved 3D case

Horizontal thermal inhomogeneities defined in Eq. (3) lead to horizontal variation of the emergent line intensity. In Fig. 1 we show the variation of the temperature and of the corresponding line-center emergent intensity in the direction $\mu = 1$ in case of two model atmospheres. For definition of the line-of-sight vector $\vec{\Omega} = (\theta, \phi)$ and the angles θ, ϕ see Fig. 2. For the cosine of the angle θ we use the standard notation $\mu = \cos \theta$.

Since the Planck function depends non-linearly on temperature, it follows that the mean Planck function at the bottom of the atmosphere, which is equal to the far-wing line intensity, depends on

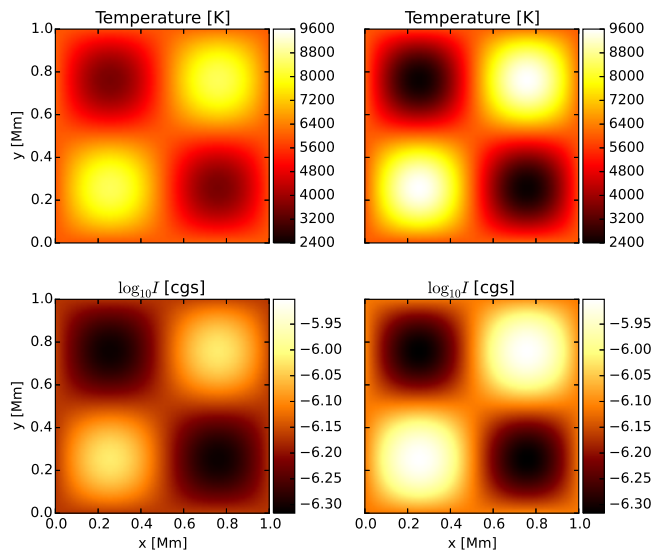


Figure 1: Top panels: variation of kinetic temperature for $\alpha_T = 0.4$ (left panel) and $\alpha_T = 0.6$ (right panel). The bottom panels show the corresponding line-center intensities in the direction along the z axis, i.e., $\mu = \cos \theta = 1$ (see Fig. 2).

the perturbation amplitude α_T . As we show below, similar effect can be found in a case of variation of the line source function at different heights of the atmosphere, which can lead to significant modification of the emergent line profile.

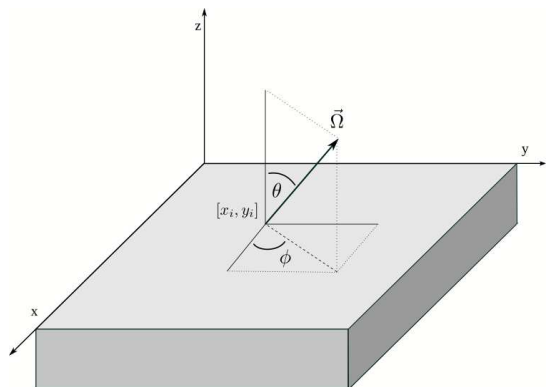


Figure 2: Definition of angles θ and ϕ of the line-of-sight vector $\vec{\Omega}$ in the cartesian coordinate system of the model.

3.2. Spatially integrated 3D case

The specific intensity of the emergent radiation $I(\vec{\Omega}, \lambda, x_i, y_j)$ is then azimuthally and spatially averaged. By doing that, we make sure that the resulting synthetic spectra contain information about horizontal inhomogeneities, which

¹Our calculations with PORTA also show that thermodynamic inhomogeneities significantly affect linear polarization of the emergent radiation. Considering the full Stokes vector (intensity, linear and circular polarization) can open more diagnostic possibilities. Polarization phenomena are, however, beyond the the scope of the present study.

are assumed to be spread across a stellar surface. The signal at each surface grid point (x_i, y_j) is integrated over azimuth $\phi \in \langle 0, 2\pi \rangle$ by performing integration (using equidistant trapezoidal rule):

$$I(\mu, \lambda, x_i, y_j) = \frac{1}{2\pi} \int_0^{2\pi} d\phi I(\vec{\Omega}, \lambda, x_i, y_j). \quad (4)$$

Thanks to the equidistant grid, the integration over the surface can be replaced by a sum, and the resulting spatially integrated synthetic spectrum is finally given as an average over all surface points (x_i, y_j) ,

$$I(\mu, \lambda) = \frac{1}{N^2} \sum_{i,j} I(\mu, \lambda, x_i, y_j) \quad (5)$$

Radiative transfer is solved for each considered frequency, thus the procedure of obtaining synthetic spectra via expressions (4) and (5) is applied for continuum intensity value as well. Despite the presence of inhomogeneities, the atmosphere is for radiation at frequencies far enough from line-center completely transparent. Therefore the continuum intensity I_C is given by lower boundary condition and is identical to the Planck function value, averaged over the very bottom layer z_0 , i.e., $I_C = \langle B(T(x, y, z_0)) \rangle_{z,y}$.

Figure 3 shows the azimuthally and spatially averaged specific intensity profiles $I(\lambda)$ computed for 3D models with inhomogeneity amplitudes $\alpha_T \in \{0.1, 0.4, 0.6, 0.8\}$ and periodicity parameter $k = 1$ (see Eq. 3), as observed at inclination $\mu = 0.1$ (close to the limb). Solid line corresponds to the case of an unperturbed (isothermal) atmosphere in planar geometry.

Figure 4 shows the inclination dependence of the azimuthally averaged specific intensity profiles $I(\lambda)$ computed for 3D model with inhomogeneity amplitude $\alpha_T = 0.6$. The peaks decrease with increasing μ (having its maximum at $\mu = 0.1$) and completely vanish for disc-center observation ($\mu = 1.0$). Intensities in Figures 3 and 4 are normalized to continuum values I_C in order to emphasize the differences in wings.

In many physically relevant cases, the emergent line intensity can be estimated using the Eddington-Barbier relation (e.g., Hubeny & Mihalas,

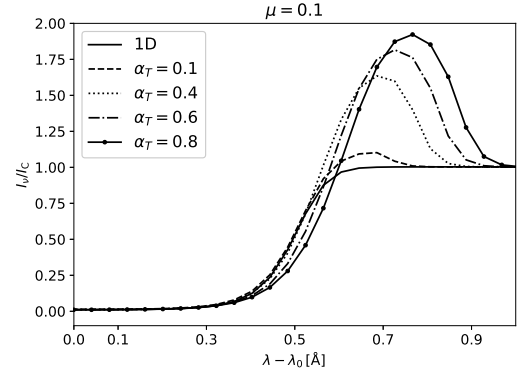


Figure 3: Influence of different temperature perturbation amplitudes α_T on spatially and azimuthally integrated emergent intensities normalized to their respective continuum values I_C . Intensities are plotted for the inclination $\mu = 0.1$. The solid line corresponds to the isothermal plane-parallel solution.

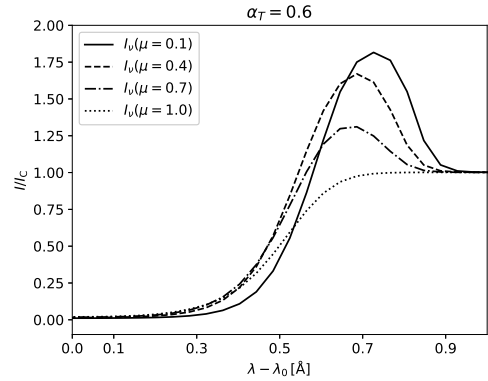


Figure 4: Emission peaks in synthetic intensity spectra appearing in solutions of inhomogeneous 3D models with temperature perturbation amplitude $\alpha_T = 0.6$ for various inclination angles. The signal has been spatially and azimuthally averaged.

2015), $I(\lambda, \mu) \approx S(\lambda, \tau_\lambda = \mu)$, where τ_λ is optical depth measured along the direction of beam propagation. The emergent radiation intensity is from atmospheric layers where the optical depth for a given wavelength and line-of-sight is around unity. The $\tau_\lambda = \mu$ surface is approximately the formation region of radiation at wavelength λ , and the Eddington-Barbier relation serves as a connection between the spectral features of line radiation and the locally calculated source function values.

Line profiles plotted in Figure 4 show that the center-to-limb variation is affected by temperature inhomogeneities as well. Observing the cor-

rugated $\tau_\lambda = \mu$ surface close to the limb (μ close to zero) means that certain areas of the surface become hidden from the line of sight, and the net intensity from visible areas may exceed the continuum value at certain wavelengths. This effect completely vanishes for observation at $\mu = 1$, since the pattern of horizontal inhomogeneities is symmetric and, on average, the contribution of rays emerging from brighter areas is balanced by rays from dimmer areas.

However, if the variation of the source function along the line of sight is significant around $\tau = 1$, the assumption of linearity of the source function with respect to optical depth no longer holds. Therefore, the Eddington-Barbier relation cannot be reliably used to predict spectral features of the emergent line radiation, and the radiative transfer solution is required. In the following, we shall explain the connection of inhomogeneities with the calculated spectra, with special emphasis on the emission peaks appearing in almost all cases of inhomogeneous 3D models.

The emission peaks at $\lambda - \lambda_0 = \Delta\lambda \approx 0.7 \text{ \AA}$ may appear only if there is a number of rays originating in regions with the source function value higher than the Planck function averaged over the horizontal domain, i.e. $S/\langle B \rangle_{x,y} > 1$ at $\tau_{\Delta\lambda=0.7} \approx \mu$. Figure 5 illustrates this and shows the source function as a function of optical thickness τ_{los} along various beams (line-of-sight) crossing the surface of the model at $y = 0.25 \text{ Mm}$ at three different surface points $x_0 = \{0.0, 0.4, 0.8\} \text{ Mm}$ with the same ray inclination $\mu = 0.4$ (left panel), and beams crossing the surface at the same point $x_0 = 0.0 \text{ Mm}$ with three various beam inclinations $\mu = \{0.1, 0.3, 0.6\}$ (right panel). The half-width of the absorption profile is proportional to the square root of temperature; regions with lower temperature are less opaque to the radiation at a given frequency. When plotted as a function of the *optical thickness* along the propagation beam, the atmospheric regions with lower temperature shrink into optically thin areas with very low values of $S/\langle B \rangle$. This causes sharp troughs in the plot.

Because of periodic horizontal boundary conditions, each beam in Fig. 5 crosses the horizon-

tal domain of the model several times according to the inclination angle, until it reaches the very bottom of the model. Figure 6 shows the source function as a function of optical thickness along the line-of-sight, computed at wavelength close to emission peaks in line-wings ($\Delta\lambda \approx 0.7 \text{ \AA}$) for 400 equally inclined beams crossing the surface of the perturbed model at random points and for four different inclinations μ .

The red lines in Fig. 6 correspond to the average over all beams, indicating that there are always positive contributions to the source function close to $\tau = 0.1$, giving higher average value of intensity than continuum. The gray areas roughly correspond to all possible values of source function along the line-of-sight.

4. Radiation flux from a spherical star

Given the lack of spatial resolution for stellar observations, we want to investigate how various temperature inhomogeneities affect the overall radiation flux emerging from a distant star, as measured by a distant observer. In the case of a non-irradiated spherical star, the emergent monochromatic specific radiation intensity integrated over the apparent stellar disk can be expressed using the monochromatic flux (see, e.g., Unsöld, 1955) as

$$F_\lambda = \frac{1}{\pi} \int_0^{2\pi} d\phi \int_0^1 d\mu \mu I_\lambda(\phi, \mu), \quad (6)$$

where $I_\lambda(\phi, \mu)$ depends on both μ and ϕ . The geometrical meaning of integration angles ϕ and θ (or equivalently ϕ and $\mu = \cos \theta$) is illustrated in Figure 7; we identify ϕ and θ with the polar angle and inclination of models calculated on the Cartesian grid as indicated in Fig. 2.

Since we calculate emergent radiation from a spherically symmetric star from planar atmospheric models, the geometry difference between planar and spherical geometry (i.e. the curvature of the spherical atmosphere) has to be taken into account. The principal difference between planar and spherical geometry is in treatment of radiation close to the limb. In planar geometry, all rays regardless the polar angle θ reach the lower

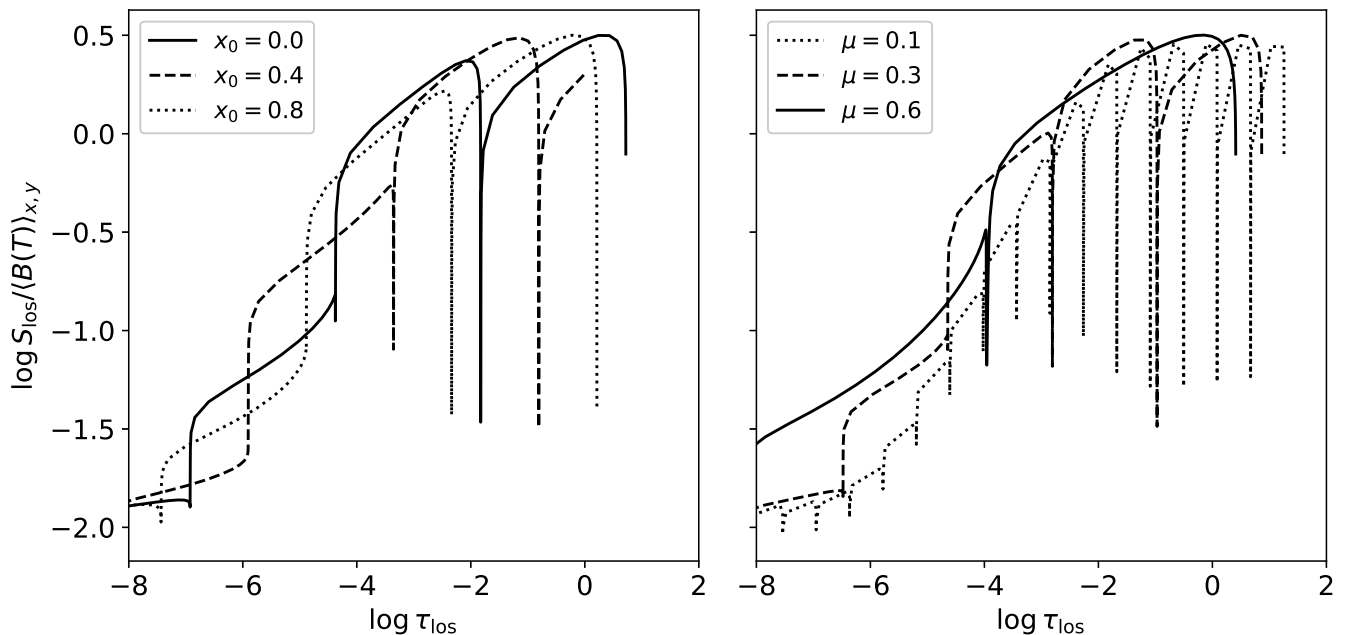


Figure 5: Source function normalized to the continuum value of intensity $\langle B(T) \rangle_{x,y}$ for various beams crossing the model surface at $y = 0.25$ Mm, namely at different points at a beam inclination $\mu = 0.4$ (left panel), and at the point $x_0 = 0.0$ Mm with various beam inclinations (right panel). Calculated for the model with temperature perturbation amplitude $\alpha_T = 0.6$, the optical thickness along the line-of-sight is calculated at $\Delta\lambda = 0.7$ Å.

boundary of the atmosphere, consequently the optically thick parts of the atmosphere. In spherical geometry, the almost tangent rays do not reach the optically thick part of the atmosphere and they emerge back at the upper boundary. As a consequence, the emergent radiation from the planar geometry is a bit overestimated for rays close to $\mu = 0$ (see Korčáková & Kubát, 2005). To correct this, we start the angle integration at $\mu = 0.1$ instead of $\mu = 0$. This way we assume that rays with the inclination in the interval $\mu \in \langle 0; 1 \rangle$ go back to infinity and do not reach the optically thick part of the atmosphere. This corresponds to the estimate that the thickness of the atmosphere is 0.5% of the stellar radius.

The integration is done in two steps. First we integrate the signal at each inclination μ over all possible azimuths $\phi \in \langle 0, 2\pi \rangle$, then the integration over $\mu \in \langle 0.1, 1 \rangle$ itself is performed (see the definition of geometry in Fig. 7). Integration over both azimuths (8 equidistantly separated directions in ϕ) and inclinations (37 equidistantly separated directions in μ) is done using the trape-

zoidal rule.

4.1. Influence of the inhomogeneity amplitude on line profiles

Fig. 8 shows the intensity profile of the radiation emerging from the horizontally perturbed 3D model with temperature inhomogeneity amplitude $\alpha_T = 0.6$ as observed close to the limb ($\mu = 0.1$) and at the disc-center ($\mu = 1.0$). Solid line corresponds to the solution of the same model, but integrated over all azimuths ϕ and inclinations $\cos\theta \equiv \mu$ as indicated by Eq. (6). Emission peaks at line wings are strongest in the case of limb observations, completely vanishing at the disc center. Interestingly, the emission still remains even after averaging over the stellar disc, which is a direct consequence of temperature inhomogeneities in atmospheric structure, mainly in its lower regions.

Fig. 9 shows the line flux calculated using Eq. (6) for inhomogeneous 3D models with different perturbation amplitudes $\alpha_T = 0.1$, $\alpha_T = 0.6$, and $\alpha_T = 0.8$. The shape of the spectral

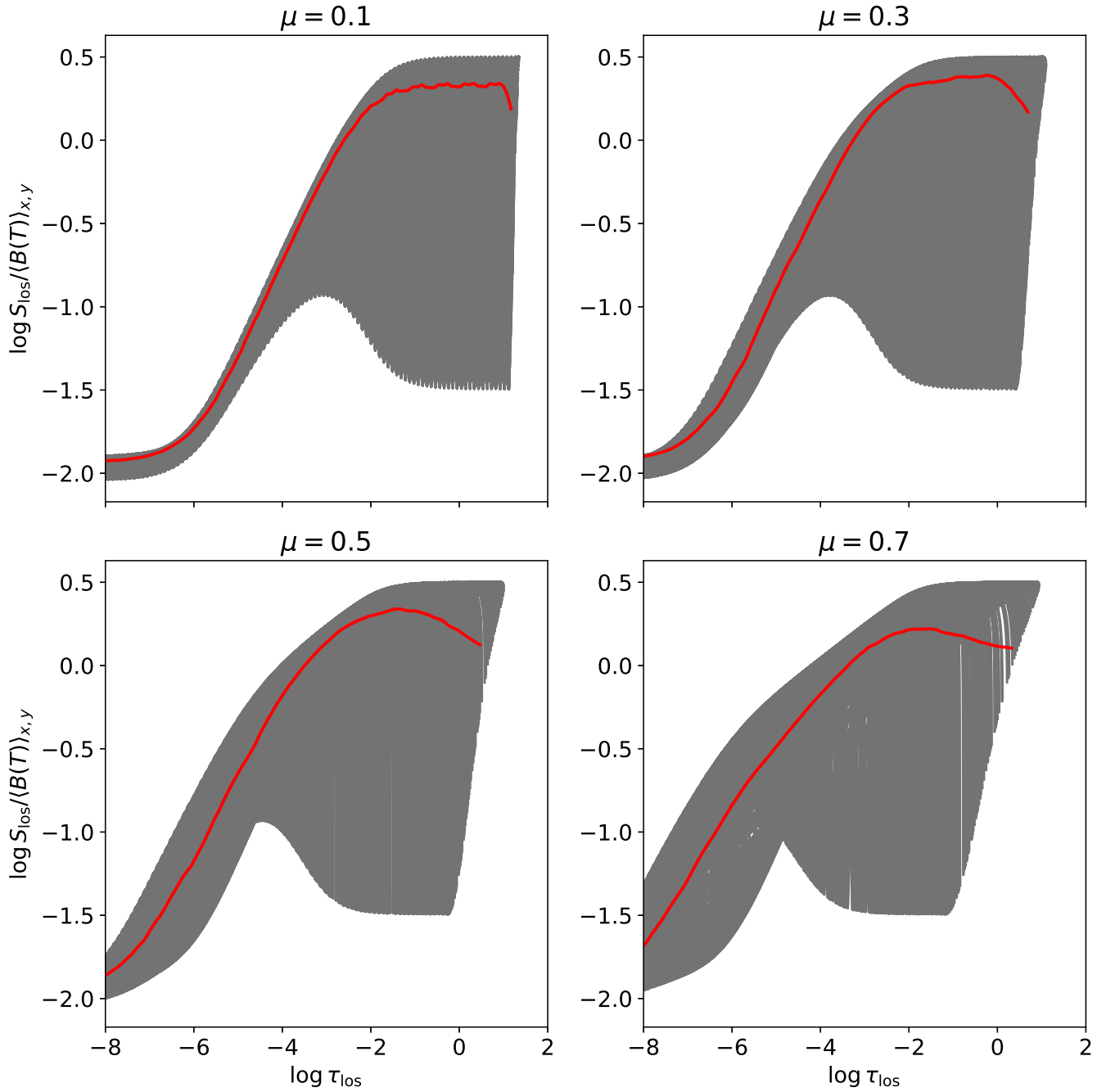


Figure 6: Source function normalized to the continuum value of intensity $\langle B(T) \rangle_{x,y}$ for 400 equally inclined rays for four different inclinations crossing the model surface at different random points X_0 , calculated for the model with temperature perturbation amplitude $\alpha_T = 0.6$. The gray area approximately corresponds to possible values of source function along the given line-of-sight. Red line corresponds to the averaged value from all plotted rays. Top panels: inclination $\mu = 0.1$ (left) and $\mu = 0.3$ (right); bottom panels: inclination $\mu = 0.5$ (left) and $\mu = 0.7$ (right).

line is, as expected, behaving similarly to the intensities shown in Fig. 3 in accordance with the value of the amplitude α_T – the overall flux increases nonlinearly with perturbation amplitude.

It is due to the strong and nonlinear temperature-dependence of the Planck function, which is coupled to the source function at $\tau_\lambda = 1$. The largest differences in flux magnitude among the plotted

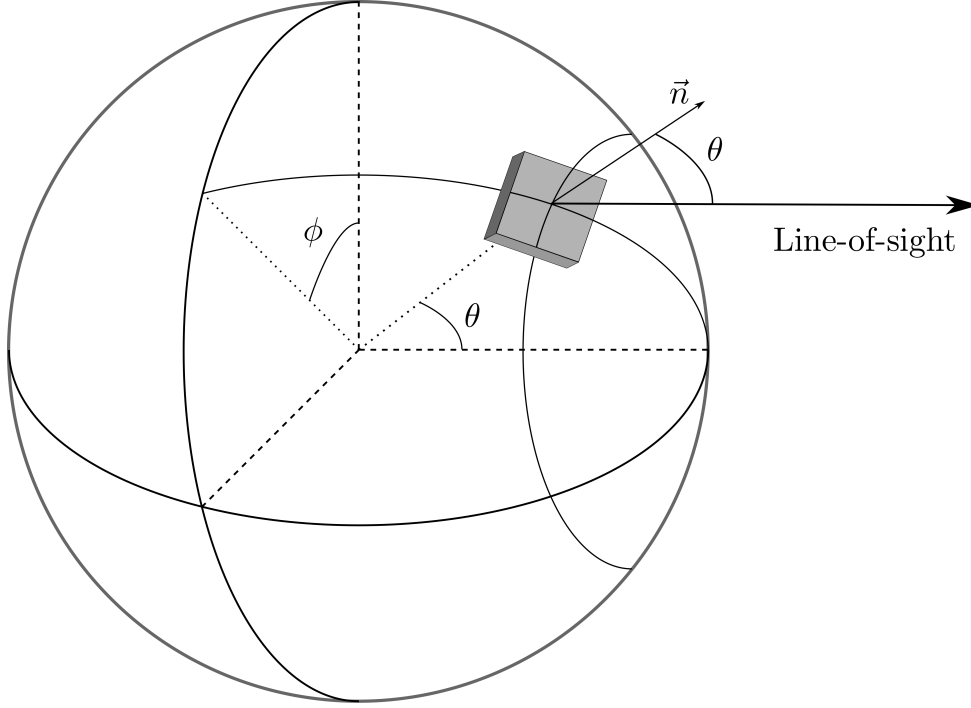


Figure 7: Geometry and definition of $\mu = \cos \theta$ and ϕ (not to scale, only sketch). The gray block illustrates the model atmosphere calculated using a 3D Cartesian grid. The stellar surface is observed from the direction of the line-of-sight, \vec{n} indicates the normal vector to the surface of the considered model. Azimuth ϕ is measured in the plane perpendicular to the line of sight.

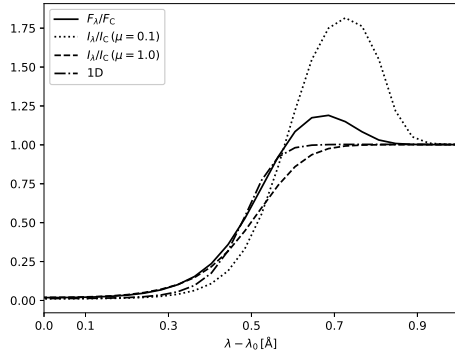


Figure 8: Intensity and flux profiles calculated for the 3D atmospheric model with horizontal temperature perturbation amplitude $\alpha_T = 0.6$. Solid line corresponds to the signal integrated over the stellar surface using Eq. (6); dashed and dotted lines correspond to the intensity of the emergent radiation from the same model, observed at inclinations $\mu = 1.0$ and $\mu = 0.1$, respectively.

models are in the line-core (formed in the upper part of the model atmosphere) and at line-wings (formed at mid- to lower model's parts). Emission peaks seems to almost vanish for the model with the smallest perturbation amplitude

$\alpha_T = 0.1$, as the temperature-driven effect is by angle-averaging for such small inhomogeneity suppressed.

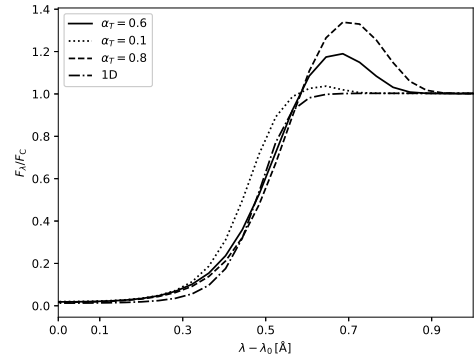


Figure 9: Profiles of the emergent flux calculated by Eq. (6) for horizontally inhomogeneous 3D atmosphere models with perturbation amplitudes $\alpha_T = 0.1$ (dotted line), $\alpha_T = 0.6$ (full line) and $\alpha_T = 0.8$ (dashed line).

4.2. Influence of the perturbation period on line profiles

The periodicity parameter k has an important impact on "visibility" of temperature inhomogeneities in calculated spectra, because it directly corresponds to its spatial scales with respect to photon destruction path ℓ^* . Fig. 10 shows results of 3D line profile calculations for three different values of the parameter k , all for the perturbation amplitude $\alpha_T = 0.6$, namely for $k = 0.1$, 1.0, and 10.0.

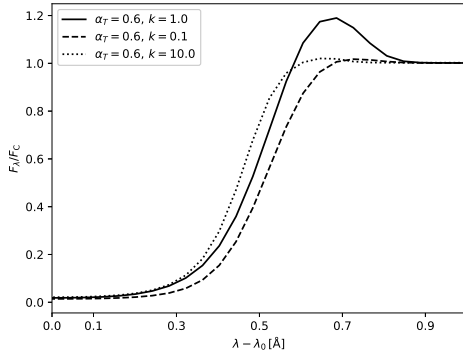


Figure 10: Emergent radiation flux calculated via Eq. (6) for horizontally inhomogeneous 3D atmosphere models with temperature perturbation amplitude $\alpha_T = 0.6$; plotted are fluxes for models with various perturbation periods: $k = 0.1$ (solid line), $k = 1.0$ (dashed line) and $k = 10.0$ (dotted line). The emission peaks remain dominant only for the model with a single perturbation period along the horizontal domain.

In the limit of low perturbation period ($k = 0.1$), the variation of temperature takes place on 10 times larger spatial scales, such that the influence of inhomogeneities on horizontal transfer of radiation becomes negligible, making the problem effectively 1.5D. Thus, we expect the emission effect at $\Delta\lambda \approx 0.7$ of the line to disappear in the spectrum of the radiation flux. On the contrary, in the limit of high perturbation period ($k = 10$), the temperature fluctuates on 10 times smaller spatial scales. Horizontal transfer of radiation effectively reduces the impact of individual inhomogeneities, causing the emission in calculated spectra to disappear.

4.3. Comparison of 1D and 3D solutions

Temperature variation along the horizontal direction of a stellar atmosphere can leave certain imprints upon the surface-integrated emergent radiation flux. However, the question about the unambiguity of the interpretation of such spectra is crucial, especially if it is used to determine the thermodynamic structure of an observed stellar atmosphere. If there exists a different atmospheric model which produces similar emergent line profiles, we are not able to decide which model better represents the atmospheric structure.

It is indeed possible to find solutions which give, to some extent, very similar spectral shape of the emergent radiation flux. Let us modify the vertical thermal structure of a plane-parallel atmosphere as a Gaussian perturbation along the z -axis of the model,

$$T(z) = T_0 \left[1 + f \exp \left(-\frac{(z - z_c)^2}{2w^2} \right) \right], \quad (7)$$

where z_c is the geometrical depth of the temperature maximum, w is a parameter influencing the width of the Gaussian profile and f is an auxiliary numerical factor reducing the maximal allowed change in temperature. Figure 11 shows an example of a vertical temperature stratification according to Eq. (7) and corresponding Planck function variation, both in relative units. The Planck function directly affects the source function at given height. The set of free parameters of the temperature structure in Fig. 11 was chosen intentionally to reproduce similar emission effects as we obtain from the horizontally inhomogeneous 3D models described in Section 3.2.

We used the trial and error strategy to obtain similar shape of the resulting line profile (i.e. emission peaks in line wings) by changing four free parameters z_c , w , f and T_0 in Eq. (7). For a given set of the free parameters we solve the NLTE problem. Then we calculate flux and compare it to the flux emerging from an inhomogeneous 3D model in consideration. While changing one parameter at a time, we figure out how each of them affects the solution.

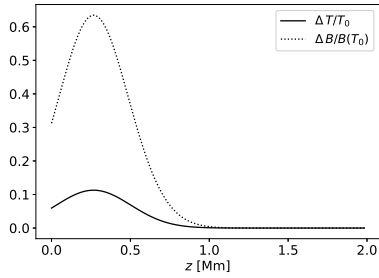


Figure 11: Vertical temperature stratification of the plane-parallel atmosphere, given by Eq. (7) with $z_c = 16$, $2w^2 = 400$, $f = 0.11$ and the reference temperature $T_0 = 6000$ K; relative change in temperature with height in the atmosphere (solid line). Dotted line corresponds to related relative change of the Planck function.

We have found several models with a vertically dependent temperature structure giving similar emission peaks in line-wings as the model with horizontal temperature perturbation, but with various differences across the wavelength range. Fig. 12 shows a line profile emerging from such vertically perturbed atmosphere, which is most similar to a profile from a horizontally inhomogeneous 3D atmosphere, equivalent in its emission maximum and slightly differing in a shape. These two similar line profiles forming in very different physical conditions serve as an example of ambiguity of emergent radiation, which may appear for stars of any spectral type.

5. Conclusions

The temperature structure of a stellar atmosphere has a significant impact on the intensity of spectral lines, which are formed at inhomogeneous regions. This is due to the presence of areas with higher values of the local source function, which tend to create higher values of intensity of a spectral line at corresponding wavelengths. This effect can influence spectra emerging from the stellar surface.

As a consequence, if we try to interpret the observed spectra using 1D atmosphere models, we can make erroneous conclusions about the atmospheric structure. A real stellar atmosphere (its spatial distribution of temperature, atomic volume density, etc.) is naturally very complicated,

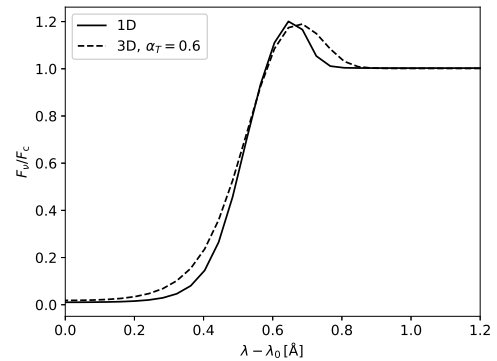


Figure 12: Radiation flux profile calculated for the horizontally inhomogeneous 3D atmosphere model with temperature perturbation amplitude $\alpha_T = 0.6$ (dashed line), obtained by applying Eq. (6). Solid line corresponds to the flux calculated for the plane-parallel atmosphere model, which gives similar spectral shape of the radiation flux. Its vertical temperature structure is given by Eq. (7) with $z_0 = 16$, $2w^2 = 400$, $T_0 = 6000$ K and $f = 0.11$.

so it is to be expected that perturbations of various origin and geometrical shape are quite common. In such a case, the multidimensional approach to the NLTE problem can provide a better tool to determine the atmospheric structure. However, it strongly depends on the nature of inhomogeneities – its shape, size and spatial distribution over the stellar surface.

Acknowledgements

The computations were performed on the parallel computer cluster OCAS at the Astronomical Institute Ondřejov. We thank Dr. J. Štěpán for the possibility to use the code PORTA and for many invaluable discussions. This research was supported by a grant GA ČR 16-01116S. The Astronomical Institute Ondřejov is supported by a project RVO:67985815 of the Academy of Sciences of the Czech Republic.

References

References

- Auer, L., Insight into Multi-Dimensional Transfer, 2003, ASPC, 288, 405.
- Cantiello, M., Langer, N., Brott, I., de Koter, A., Shore, S. N., Vink, J. S., Voegler, A., Lennon, D. J., & Yoon,

- S.-C., Sub-surface convection zones in hot massive stars and their observable consequences, 2009, *A&A*, 499, 279
- Chiueh, T., Fluctuations in Stellar Winds and Their Possible Connections to the Wind Mass Flux, 1997, *ApJ*, 482, L179
- Cram, L. E., Radiative transfer in geometries other than plane-parallel layers, 1977, *MmSAI*, 48, 377
- Hubeny, I. & Mihalas, D., *Theory of Stellar Atmospheres*, 2015, Princeton University Press, New Jersey.
- Ibgui, L., Hubeny, I., Lanz, T., & Stehlé, C., IRIS: a generic three-dimensional radiative transfer code, 2013, *A&A*, 549, A126.
- Korčáková, D., & Kubát, J., Radiative transfer in moving media. II. Solution of the radiative transfer equation in axial symmetry, 2005, *A&A*, 440, 715.
- Leenaarts, J., Pereira, T. M. D., Carlsson, M., Uitenbroek, H., De Pontieu, B., The Formation of IRIS Diagnostics. I. A Quintessential Model Atom of Mg II and General Formation Properties of the Mg II h&k Lines, 2013a, *ApJ* 772, 89.
- Leenaarts, J., Pereira, T. M. D., Carlsson, M., Uitenbroek, H., De Pontieu, B., The Formation of IRIS Diagnostics. II. The Formation of the Mg II h&k Lines in the Solar Atmosphere, 2013b, *ApJ* 772, 90.
- Oskinova, L. M., Kubátová, B., & Hamann, W.-R., Moving inhomogeneous envelopes of stars, 2016, *JQSRT*, 183, 100.
- Owocki, S. P., Castor, J. I., & Rybicki, G. B., Time-dependent models of radiatively driven stellar winds. I - Nonlinear evolution of instabilities for a pure absorption model, 1988, *ApJ*, 335, 914
- Štěpán, J., & Trujillo Bueno, J., PORTA: A three-dimensional multilevel radiative transfer code for modeling the intensity and polarization of spectral lines with massively parallel computers, 2013, *A&A*, 557, A143.
- Sundqvist, J. O., Owocki, S. P., & Puls, J., The Nature and Consequences of Clumping in Hot, Massive Star Winds, 2012, *ASP Conf. Ser.* 465, 119
- Šurlan, B., Hamann, W.-R., Kubát, J., Oskinova, L. M., & Feldmeier, A., 3-D radiative transfer in clumped hot star winds I. Influence of clumping on the resonance line formation, 2012, *A&A*, 541, A37.
- Šurlan, B.; Hamann, W.-R.; Aret, A.; Kubát, J.; Oskinova, L. M.; Torres, A. F., Macroclumping as solution of the discrepancy between H α and P v mass loss diagnostics for O-type stars, 2013, *A&A*, 559, A130
- Uitenbroek, H., & Criscuoli, S., Why One-dimensional Models Fail in the Diagnosis of Average Spectra from Inhomogeneous Stellar Atmospheres, 2011, *ApJ*, 736, 69.
- Unsöld, A., *Physik der Sternatmosphären*, 2nd ed., 1955, Springer Verlag Berlin.